Article

Size effect analysis of quasi-brittle fracture with localizing gradient damage model

Yi Zhang[1] ⓘ, Amit S. Shedbale[1,2], Yixiang Gan[3],
Juhyuk Moon[4] and Leong H. Poh[1] ⓘ

Abstract

The size effect of a quasi-brittle fracture is associated with the size of fracture process zone relative to the structural characteristic length. In numerical simulations using damage models, the nonlocal enhancement is commonly adopted to regularize the softening response. However, the conventional nonlocal enhancement, both integral and gradient approaches, induces a spurious spreading of damage zone. Since the evolution of fracture process zone cannot be captured well, the conventional nonlocal enhancement cannot predict the size effect phenomenon accurately. In this paper, the localizing gradient enhancement is adopted to avoid the spurious spreading of damage. Considering the three-point bend test of concrete beams, it is demonstrated that the dissipation profiles obtained with the localizing gradient enhancement compare well with those of reference meso-scale lattice models. With the correct damage evolution process, the localizing gradient enhancement is shown to capture the size effect phenomenon accurately for a series of geometrically similar concrete beams, using only a single set of material parameters.

Keywords

Quasi-brittle fracture, size effect, localizing gradient damage, concrete

Introduction

The size effect of quasi-brittle fracture is widely reported, yet it is difficult to capture this phenomenon numerically with continuum damage models. During strain softening, the structural response is largely driven by the development and propagation of the fracture process zone (FPZ). Since the size of this FPZ does not scale consistently with the characteristic dimension of geometrically similar

[1]Department of Civil and Environmental Engineering, National University of Singapore, Singapore, Singapore
[2]Department of Mechanical Engineering, Indian Institute of Technology (BHU), Varanasi, India
[3]School of Civil Engineering, The University of Sydney, Sydney, Australia
[4]Department of Civil and Environmental Engineering, Seoul National University, Seoul, South Korea

Corresponding author:
Leong H. Poh, Department of Civil and Environmental Engineering, National University of Singapore, Block E1A, Level 07, Room 03, 1 Engineering Drive 2, (S)117576, Singapore, Singapore.
Email: ceeplh@nus.edu.sg

specimens, a size effect is induced at the structural level. Numerically, conventional nonlocal integral and gradient enhancements are commonly adopted to regularize the structural strain softening responses. However, the damage process zone suffers from spurious numerical artifacts. Consequently, conventional nonlocal enhancements cannot capture the size effect phenomenon satisfactorily. This motivates the present paper, where the so-called localizing gradient enhancement is shown to capture the size effect naturally.

Quasi-brittle structures exhibit two main types of size effects based on characteristics of the FPZ, which in turn is influenced by the nature of specimen boundary. This was discussed extensively in the context of notched and unnotched concrete beams in three-point bend tests (Barbat et al., 2020; Bažant and Le, 2017; Bažant and Planas, 1997; Bažant and Yu, 2009; Hoover and Bažant, 2014). A Type 1 size effect is observed with unnotched beams, where distributed microcracks formed within a large process zone at peak load, and structural failure occurring with the initiation of a macroscopic crack. With deeply notched beams, the maximum load is associated with the development of a long macro-crack to give a Type 2 size effect. An extensive experimental design with notches of varying depths was reported to investigate the transition between Type 1 and 2 size effects (Grégoire et al., 2013; Hoover et al., 2013).

Numerically, standard continuum damage models are mesh dependent during strain softening. One popular remedy is to adopt either a nonlocal integral or gradient enhancement, where a nonlocal variable is utilized to drive the damage process. In the former approach, this nonlocal variable is obtained via the weighted spatial average of the local counterpart within an interaction domain (Pijaudier-Cabot and Bažant, 1987). For the latter, the local variable serves as a source term in a differential equation that governs the evolution of the nonlocal term, with a length scale parameter characterizing the size of the interaction domain (Al-Rub and Voyiadjis, 2009; Peerlings et al., 1996, 1998, 2001). The gradient approach can be understood as a reformulation of the integral enhancement (Peerlings et al., 2001).

In a nonlocal enhancement, the interaction domain characterizes the size of FPZ. While the structural strain softening response is now regularized, conventional nonlocal enhancements induce numerical artifacts in the damage process zone. This was first reported in the context of conventional gradient enhancement in Geers et al. (1998) where a spurious spreading of damage bandwidth was shown. Other artifacts include an incorrect description of crack initiation and propagation process (Geers et al., 1998; Simone et al., 2004). Similar issues were reported with the conventional nonlocal integral enhancement (Giry et al., 2011; Nguyen, 2011). Recall that the development and evolution of FPZ underpin the two types of size effects. Since conventional nonlocal enhancements cannot describe the evolution and propagation of damage process zones correctly, they are inadequate in capturing both types of size effects. This limitation was reported extensively for the integral approach (Grégoire et al., 2013; Havlásek et al., 2016; Marzec and Bobiński, 2019a), and briefly illustrated for the gradient approach in Wosatko et al. (2018).

The spurious effects in conventional nonlocal enhancements arise due to the assumption of a constant interaction domain size through the loading history, which enforces a diffusion of active damage processes to the neighboring regions - see discussions in Poh and Sun (2017). In the context of conventional integral enhancement, much attention has been focused on a so-called boundary effect induced by this spurious diffusion of damage process zone to regions below the notch tip/ macro-crack. To this end, modifications were made to the averaging function to "sense" the boundaries, e.g. in the stress based (Giry et al., 2011; Grassl et al., 2014), distance based (Grassl et al., 2014; Havlásek et al., 2016) and local complement (Grassl et al., 2014; Jirásek et al., 2004) integral formulations. It is also worth mentioning here that other enhanced formulations, such as the phase-field regularized cohesive zone model (Feng and Wu, 2018) and the thick level set damage model

(Gómez et al., 2017), were shown to capture both types of size effects well without undue calibrations. Compared to conventional nonlocal enhancements, the phase-field and thick level set approaches do not suffer from the spurious damage growth phenomenon. Other attempts to achieve localized failure include the thermodynamics-based framework recently proposed by Nguyen and Bui (2020). Results suggest that a proper development and propagation of damage process zone, without spurious effects, can resolve the limitations of conventional nonlocal enhancement for size effect predictions.

This sets the backdrop of the current presentation, on the localizing gradient enhancement proposed in Poh and Sun (2017). Departing from the conventional gradient formulation, an interaction function that decreases with damage was incorporated into a micromorphic framework for damage models (Forest, 2016, 2009), to recover a balance equation that closely resembles the conventional gradient expression. The localizing gradient enhancement was shown to avoid the spurious effects for quasi-static fracture (Poh and Sun, 2017; Sarkar et al., 2019), dynamic fracture (Wang et al., 2019) and ductile fracture (Xu et al., 2020; Xu and Poh, 2019). It has also shown to work well for the failure of fiber-reinforced epoxy (Nguyen et al., 2019) and corrosion induced damage of concrete (Seetharam et al., 2019). It is thus of interest to investigate the capability of the localizing gradient enhancement, in capturing the two types of size effects.

The paper is structured as follows. An isotropic damage model and the localizing gradient enhancement are briefly introduced in second section. The spurious spreading and boundary effects of the conventional gradient enhancement are elaborated in third section, which are shown to be resolved with the localizing gradient enhancement in fourth section. Finally, the localizing gradient enhancement is adopted for the series of three-point bend tests of concrete beams in Hoover et al. (2013), and its predictive capability demonstrated for both types of size effects in fifth section.

Localizing gradient enhanced damage model

In this work, a simple isotropic damage model is adopted, with a gradient enhancement to regularize its softening response. A brief outline is provided below. Details can be found at Poh and Sun (2017).

The constitutive law is given by

$$\boldsymbol{\sigma} = (1 - \omega)\boldsymbol{\mathcal{C}} : \boldsymbol{\varepsilon} \tag{1}$$

where $\boldsymbol{\sigma}$ is the stress, $\boldsymbol{\varepsilon}$ denotes the strain and $\boldsymbol{\mathcal{C}}$ is the elastic stiffness tensor. ω is a scalar damage variable characterizes the degradation process. A detailed discussion on possible choices of the damage variable can be found in Voyiadjis and Kattan (2009). Note that the constitutive law in (1) should rightfully include a coupling stress component based on the micromorphic framework. It was, however, set as a negligible term in Poh and Sun (2017), to recover the standard constitutive relation. In this paper, the standard constitutive relation (1) will be adopted directly.

Assuming a deformation driven damage process, the damage variable (ω) is defined in terms of a deformation history variable κ such that

$$0 \leq \omega(\kappa) \leq 1, \quad \kappa(t) = \max\{\tilde{e}(\tau) | 0 \leq \tau \leq t\} \tag{2}$$

where t is the loading step. The scalar variable $\tilde{e}$ is a micromorphic kinematic field that characterizes the deformation at the micro-scale.

At the macro-scale, the deformation is characterized via an equivalent strain measure e. In this paper, we adopt the Rankine equivalent strain (Jirásek, 2004)

$$e = \sqrt{\sum_{I=1}^{3} \langle \bar{\sigma}_I \rangle^2} \tag{3}$$

where $\langle \ \rangle$ is the Macaulay bracket; $\bar{\sigma}_I$, $I = 1, 2, 3$ are the principal values of effective stress tensor $\boldsymbol{\sigma}_e = \mathcal{C} : \boldsymbol{\varepsilon}$.

Based on the generalized micromophic framework (Poh and Sun, 2017), the microforce balance governing the micro-macro interactions is given by

$$\tilde{e} - e = \nabla \cdot \left(g l^2 \nabla \tilde{e} \right) \tag{4}$$

where l is the length scale parameter characterizing the size of damage process zone. To account for the decreasing bandwidth of active micro-cracks during the formation of a macro localized crack, the interaction function g is defined in terms of damage such that

$$g = g(\omega) = \begin{cases} 1, & \omega = 0 \\ R, & \omega \to 1 \end{cases} \tag{5}$$

where $R \approx 0$ is a residual interaction value. Note that the conventional gradient enhancement is recovered for the special case where $g = 1$, a constant interaction domain persists throughout the deformation process.

In general, different interaction functions can be proposed. Here, we follow that Poh and Sun (2017) to set

$$g = \frac{(1 - R)\exp(-\eta\omega) + R - \exp(-\eta)}{1 - \exp(-\eta)} \tag{6}$$

where η is a material parameter that controls the rate of decrease in the interaction domain during the failure process. The influence of residual value R and parameter η on the interaction function, and the corresponding structural response, can be found in Sarkar et al. (2019).

Given that the limited thickness of the concrete specimens for all the examples, plane stress state is assumed in our work. Hence, the Rankine equivalent strain in (3) becomes

$$e = \frac{1}{E} \sqrt{\langle \bar{\sigma}_1 \rangle^2 + \langle \bar{\sigma}_2 \rangle^2} \tag{7}$$

where

$$\begin{aligned}
\bar{\sigma}_1 &= 0.5(\sigma_{xx} + \sigma_{yy} + S), \\
\bar{\sigma}_2 &= 0.5(\sigma_{xx} + \sigma_{yy} - S), \\
S &= \sqrt{(\sigma_{xx} - \sigma_{yy})^2 + 4\sigma_{xy}^2}, \\
\mathcal{C} &= \frac{E}{1 - v^2} \begin{bmatrix} 1 & v & 0 \\ v & 1 & 0 \\ 0 & 0 & \dfrac{1 - v}{2} \end{bmatrix}
\end{aligned}$$

In the literature, an exponential damage evolution law is generally preferred to give a more stable numerical framework, since a complete loss of material stiffness is avoided. For convenience, we will likewise adopt the commonly used exponential damage evolution law (Mazars and Pijaudier-Cabot, 1989; Peerlings et al., 1998) below

$$\omega = \omega(\kappa) = \begin{cases} 0 & \text{if} \quad \kappa < \kappa_0 \\ 1 - \dfrac{\kappa_0}{\kappa}\left\{1 - \alpha + \alpha\exp\left[-\beta(\kappa - \kappa_0)\right]\right\} & \text{if} \quad \kappa \geq \kappa_0 \end{cases} \tag{8}$$

where κ_0 is a threshold value beyond which damage occurs, with α and β as the damage parameters. The parameter β controls the rate of damage growth, while parameter α defines the residual stress in uniaxial tension as $(1 - \alpha)E\kappa_0$ (Peerlings et al., 1998).

In this paper, plane stress condition will be assumed for all problems considered. The corresponding 2D numerical framework for the damage model is provided in Appendix 1. Throughout this paper, $\eta = 5$, $R = 0.005$ and $\alpha = 1$ are utilized.

Spurious effects with conventional gradient enhancement

In this paper, we focus on the size effect phenomenon in the three-point bend test of concrete beams, which is characterized by the relative size between FPZ and beam depth. Depending on the FPZ characteristics, a Type 1 or 2 size effect is observed (Grégoire et al., 2015; Marzec and Bobiński, 2019a). Correspondingly, a numerical model has to capture the evolution and propagation of FPZ correctly, in order to predict the size effect accurately. In the context of the conventional nonlocal integral enhancement, much work has been reported on its inadequacy for structural size effect predictions, i.e. the structural responses of geometrically similar concrete beams cannot be accurately reproduced with a single set of material parameters, for both elasticity-based isotropic damage models (Grégoire et al., 2013; Havlásek et al., 2016) and elasto-plasticity models (Marzec and Bobiński, 2019a).

It is largely accepted that the conventional nonlocal integral approach induces a "boundary effect" which results in an artificial strengthening above the notch tip. This can be best illustrated by considering a notched beam. The averaging function in the conventional nonlocal integral approach enforces a diffusion of damage in the active process zone, to the neighboring regions within the interaction domain, including material points *below* the notch tip. Hence, the numerical process zone includes regions below the notch tip, which is not physical. This boundary effect induces an artificial strengthening mechanism in the "true" process zone above the notch tip, since a larger dissipation is now required for the evolution and/or propagation of damage therewith (Grassl et al., 2014; Havlásek et al., 2016).

To address this limitation, several modified averaging procedures have been proposed for a better "sensing" of the boundary, e.g. (i) the stress-based approach (Giry et al., 2011; Grassl et al., 2014), where the influence of the boundary on a specific material point is implicitly perceived by its stress state; (ii) the distance-based approach (Grassl et al., 2014; Havlásek et al., 2016), where the averaging function at a point is scaled according to its distance to the nearest boundary; (iii) the local-complement method (Grassl et al., 2014; Jirásek et al., 2004), where the contribution of the losing material outside the physical boundaries is preserved by a "fixed" averaging function with an additional term. Comparing the dissipation profiles for notched specimens with meso-scale lattice models, the stress-based, distance-based and local-complement averaging approaches are shown to reduce the spurious dissipation close to the notch (Grassl et al., 2014). In terms of size effect
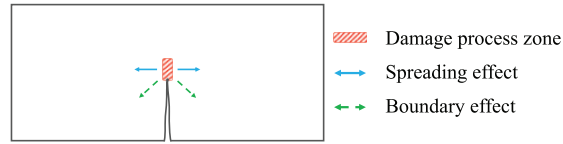
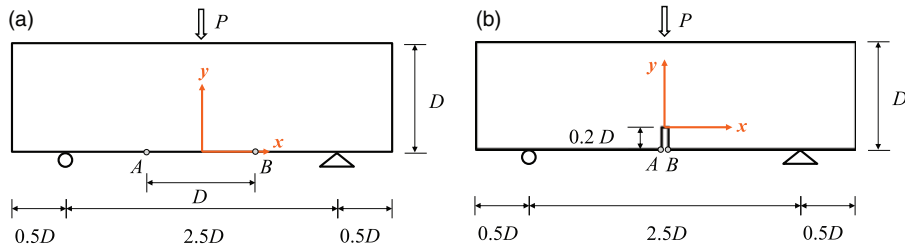**Figure 1.** The "spreading" and "boundary" effects induced in the damage process zone.

Figure 2. Geometry and test set up for the (a) unnotched specimen with $D = 100$ mm and (b) notched specimen with $D = 200$ mm, $\lambda = 0.2$ and a notch width of 2 mm. The out-of-plane thickness for both specimens is 50 mm.

predictions, the distance-based averaging approach is able to provide good predictions (Havlásek et al., 2016), while the stress-based averaging approach continues to over-estimate the peak forces (Giry et al., 2014; Marzec and Bobiński, 2019b).

The conventional gradient enhancement suffers from the same spurious damage growth phenomenon, and is equally inapt for size effect analyses. This was demonstrated by Wosatko et al. (2018), where the experimentally observed size effect in Grégoire et al. (2013) for unnotched specimens cannot be captured properly with a single set of parameters. In the following, the mechanisms underlying the limitations of conventional gradient enhancement are elaborated.

For ease of discussion, we distinguish between two interconnected, yet subtly different mechanisms, as depicted in Figure 1: (i) a spreading effect that retards the localization process; (ii) a boundary effect – following the terminology in the integral approach – where damage spreads towards physical notches/cracks. It is highlighted that available discussions with the nonlocal integral approach mostly focus on the boundary effect only.

In the following, we consider an unnotched ($\lambda = 0$) beam and a notched ($\lambda = 0.2$) beam in the three-point bend tests by Grégoire et al. (2013), where λ denotes the notch to beam depth ratio. The geometrical details of the two beams considered are shown in Figure 2. The concrete properties obtained experimentally are $E = 37$ GPa and $\nu = 0.21$. In the numerical model, the damage initiation threshold is calibrated as $\kappa_0 = 0.72 \times 10^{-4}$. For the two beams considered here, Grégoire et al. (2015) characterized the damage evolution process via meso-scale simulations using 2D lattice model, where concrete is assumed as a three-phase material comprising of coarse aggregate, mortar matrix and interfacial layer. The meso-scale 2D lattice model was reported to capture the size effect phenomenon well (Grassl et al., 2012). Thus, the meso-scale dissipation profiles are taken as reference solutions for benchmarking the performance of the gradient enhancements.

Unnotched specimen

We first consider the unnotched specimen in Figure 2(a), where the crack mouth opening displacement (CMOD) is defined as the relative horizontal distance between points A and B. The length
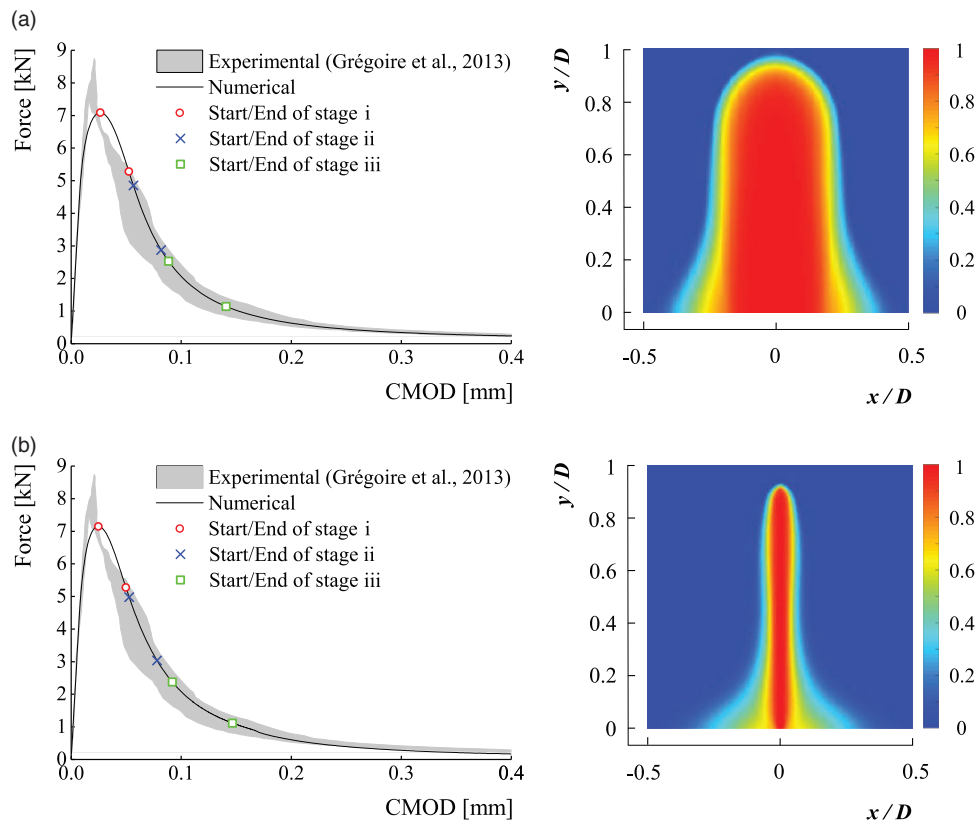
Figure 3. Numerical structural response compared to experimental data (Grégoire et al., 2013) for unnotched specimen, and the corresponding damage profile at CMOD = 0.2 mm with (a) conventional gradient enhancement ($l = 5$ mm, $\beta = 750$); (b) localizing gradient enhancement ($l = 5$ mm, $\beta = 60$).

scale parameter is assumed as $l = 5$ mm, and the corresponding softening parameter β is calibrated as 750, to fit the structural response with respective to the experimental data in Figure 3(a). The absence of a pre-existing notch in this example enables us to focus solely on the spreading effect, as per the definition introduced in Figure 5(a).

The damage profile at the final stage of loading is presented on the right side of Figure 3(a). Note that the damage bandwidth is about 50 mm, despite adopting a small length scale parameter of $l = 5$ mm in the gradient enhancement. This already suggests a spreading effect, which will be further illustrated below.

As reported in Grégoire et al. (2015), the structural behavior and the dissipation within the damage process zone for concrete beams tested in Grégoire et al. (2013) were numerically analyzed with the meso-scale 2 D lattice model. Note that the analysis results for each specimen were presented as the average values from 10 different random realizations. Therewith, the projections of the incremental dissipation in the vertical direction were extracted from the meso-scale analyses at three different loading stages. At each loading step, the dissipation histograms along the ligament length is obtained by integrating the spatial incremental dissipation density in the horizontal direction. The meso-scale results are presented in Figure 4, which will be used for benchmarking the performance of the gradient damage models in this paper.
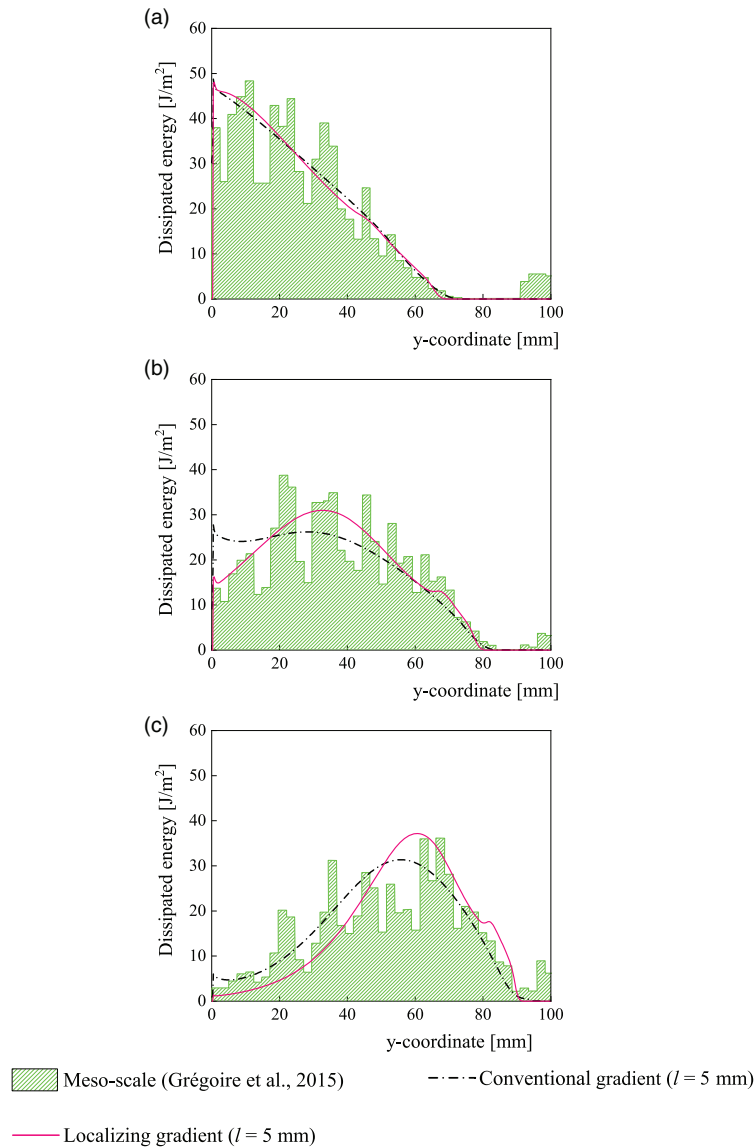
Figure 4. Vertical projections of incremental dissipation for the unnotched specimen using conventional (dash dot line) and localizing (solid line) gradient enhancements with $l = 5$ mm, compared against corresponding projected incremental dissipation histograms from meso-scale lattice model (Grégoire et al., 2015) at the three loading stages of Figure 3(a) and (b), respectively.

Following the meso-scale analysis in Grégoire et al. (2015), three loading intervals with the same amount of incremental dissipation are considered here, as depicted in Figure 3(a). The incremental dissipation profiles projected in the vertical direction, for the conventional gradient enhancement, are plotted alongside the dissipation histograms from the meso-scale analyses for the three loading stages. Details on the determination of dissipation profile is provided in Appendix 2. It is easily
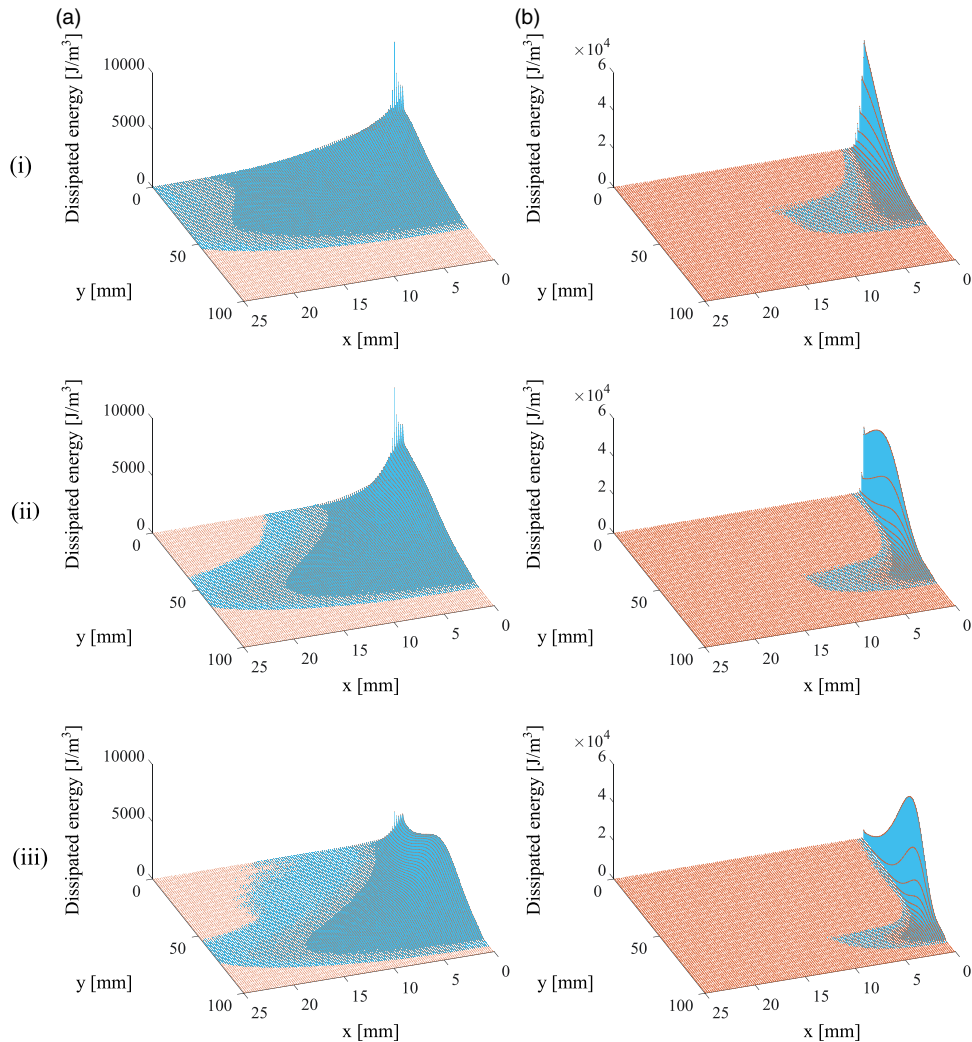
Figure 5. Dissipation maps of the unnotched specimen using (a) conventional gradient enhancement ($l = 5$ mm); (b) localizing gradient enhancement ($l = 5$ mm), at the three loading stages of Figure 3(a) and (b), respectively. Only half of the specimen is presented due to symmetry.

observed that spurious dissipation spikes are not readily observed at the specimen boundary ($y = 0$), which is consistent with our earlier point that an unnotched specimen does not exhibit any boundary effect as defined in Figure 1. Note that the projected dissipation profiles in Grassl et al. (2014), obtained from conventional integral enhancement, similarly do not exhibit any spikes at the boundary of unnotched specimen.

Although the projected profiles in Figure 4 from the conventional gradient enhancement seem to match well with the meso-scale histograms, a clear spreading effect can be observed from the incremental dissipation map shown in Figure 5(a). Throughout the strain softening process, a

large active FPZ is obtained with the conventional gradient enhancement. Note that this spreading effect is a well known limitation of the conventional gradient enhancement (Geers et al., 1998; Simone et al., 2004; Sun and Poh, 2016).

Notched specimen

The three-point bend of notched specimen as depicted in Figure 2(b) is considered in this section. Referring to Figure 1, we expect to see a boundary effect, in addition to the spreading effect observed earlier for the unnotched beam. The same parameters as before are adopted here, except for a recalibration of $\beta = 700$ such that the softening response matches the experimental data in Figure 6(a). The fact that β has to be recalibrated here already highlights the limitation of conventional gradient enhancement, i.e. a single set of material parameters cannot be used to capture correctly the size effect phenomenon.

The damage profile at the final loading stage shown in Figure 6(a) also provides a quick illustration of the spurious effects: a spreading effect leading to a broad damage bandwidth of 50 mm, despite utilizing a small length scale parameter of only 5 mm, which is inconsistent with experimental observations for notched specimens (e.g. see Figure 15(b) for a notched beam with similar λ value); a boundary effect where significant damage develops below the crack tip. These artifacts are elaborated below.

As before, the incremental dissipation at three loading stages are projected in the vertical direction and depicted in Figure 7(a), compared against the corresponding histograms from the meso-scale lattice models by Grégoire et al. (2015). A sharp spike in the dissipation is observed at the notch tip ($y = 0$), especially at the earlier stages of the softening process. A closer look near the notch tip in Figure 7(b) indicates spurious dissipation *below* the notch. This boundary effect is consistent with that reported for the conventional integral approach, e.g. a high dissipation spike has been observed in Grassl et al. (2014) for the total dissipation analysis of a sharp-notched specimen. The study also reveals that while the other modified integral approaches (i.e. the stress-based, distance-based and the local implement methods) improve the boundary effect by having a smaller peak near the notch tip, a spreading effect *below* the notch is still obtained.

As mentioned earlier, most analyses with the conventional integral approach focus only on the boundary effect. Here, we highlight the presence of an accompanying spreading effect, depicted in Figure 8(a). The boundary effect is observed clearly from the dissipation spikes at the notch tip, as well as the spurious dissipation below the notch. In addition, we observe a very wide bandwidth of the dissipation map in the horizontal (x) direction, i.e. a spreading effect.

The boundary effect artificially strengthens the notch tip, as a larger dissipation is now required for crack initiation. The spreading effect retards the crack propagation process, by smearing the dissipation across a larger bandwidth. The combined influence on the crack initiation and propagation processes can be observed in Figure 9(a), where only a small crack is captured at peak load F_{max} and a diffused macro-crack with a relative fracture length of $L_{crack}/D \approx 0.25$ at $80\% F_{max}$ post peak. This is inconsistent with the observation in Alam et al. (2014), where the evolution of fracture length of a notched specimen with similar geometry ($D = 200$ mm, $\lambda = 0.2$ and span $= 3D$) examined using the digital image correlation (DIC) technique showed a crack length developing from the notch of $L_{crack}/D = 0.2$ at peak load, which propagated quickly to $\sim$0.45 at $80\% F_{max}$ post peak. A similar observation is also reported in the DIC results of Moazzami et al. (2020) for notched specimens from cohesive frictional materials (marble and sandstones), i.e. a confined FPZ accompanied by a rapid development of macroscopic crack near F_{max}.
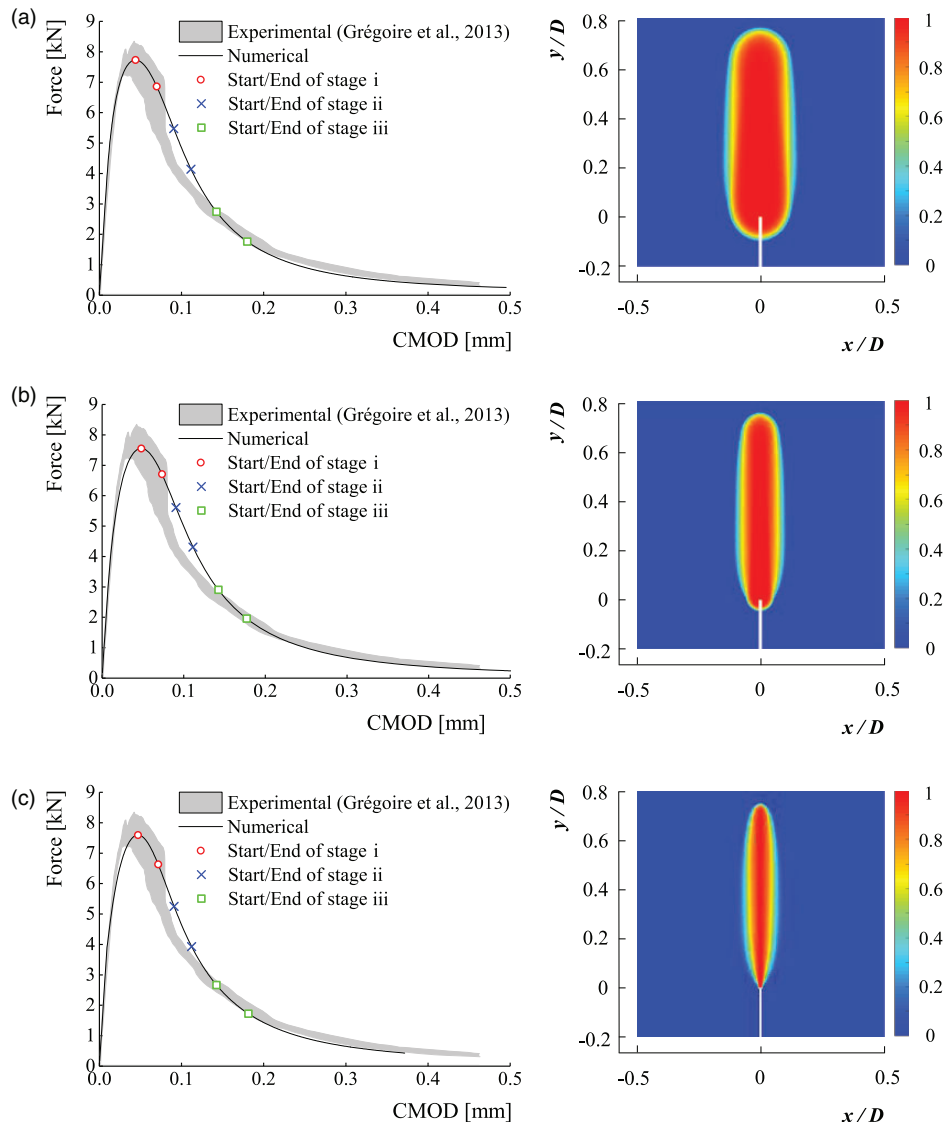
Figure 6. Numerical structural response compared to experimental data (Grégoire et al., 2013) for notched specimen, and the corresponding damage profile at CMOD = 0.3 mm with (a) conventional gradient enhancement ($l = 5$ mm, $\beta = 700$); (b) conventional gradient enhancement ($l = 2$ mm, $\beta = 280$); (c) localizing gradient enhancement ($l = 5$ mm, $\beta = 60$).

A smaller length scale parameter. The length scale parameter characterizes the size of interaction domain. In this section, we investigate the effectiveness of having a smaller length scale parameter, as a quick remedy to control the boundary and spreading effects. The same notched problem in Figure 2(b) is considered, with $l = 2$ mm and $\beta = 280$, to give a structural response in Figure 6(b) that matches the experimental data. Compared to Figure 6(a), the damage profile in Figure 6(b) exhibits
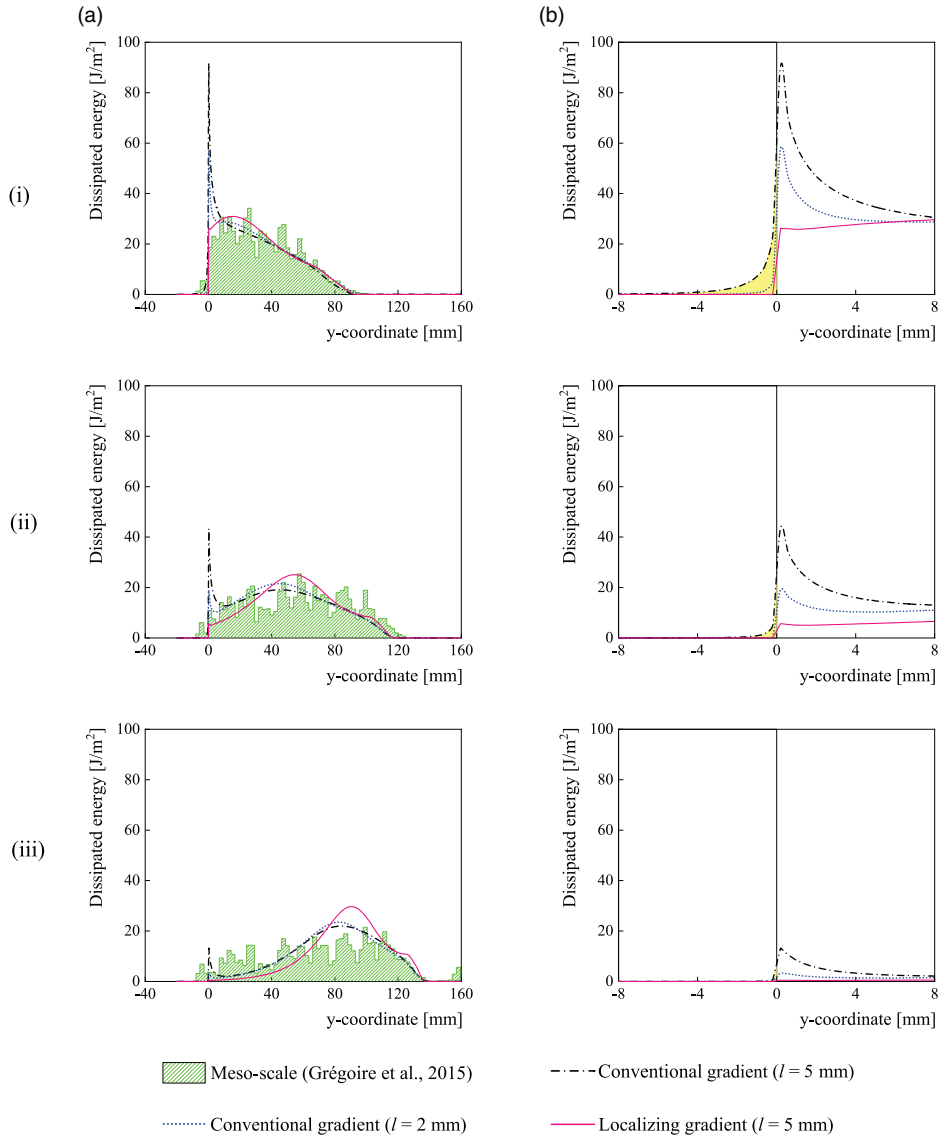
Figure 7. (a) Vertical projections of incremental dissipation for the notched specimen, compared against corresponding projected incremental dissipation histograms from meso-scale lattice model (Grégoire et al., 2015), with the conventional gradient enhancement of $l = 5$ mm, $l = 2$ mm and localizing gradient enhancement of $l = 5$ mm, at the three loading stages of Figure 6(a), (b) and (c) respectively. (b) The zoom in of spurious incremental dissipation below the notch tip (shaded region) at each loading step with the conventional gradient enhancement.

a narrower bandwidth, though it is still larger than the experimentally observed fracture process bandwidth for a similar notched beam in Figure 15(b).

As depicted in Figure 7, the boundary effect with a smaller length scale parameter is reduced, compared to the earlier case with $l = 5$ mm. Particularly, the spike in dissipation at the notch tip persists only at the initial softening stage, with a smaller spread below the notch tip ($y < 0$).
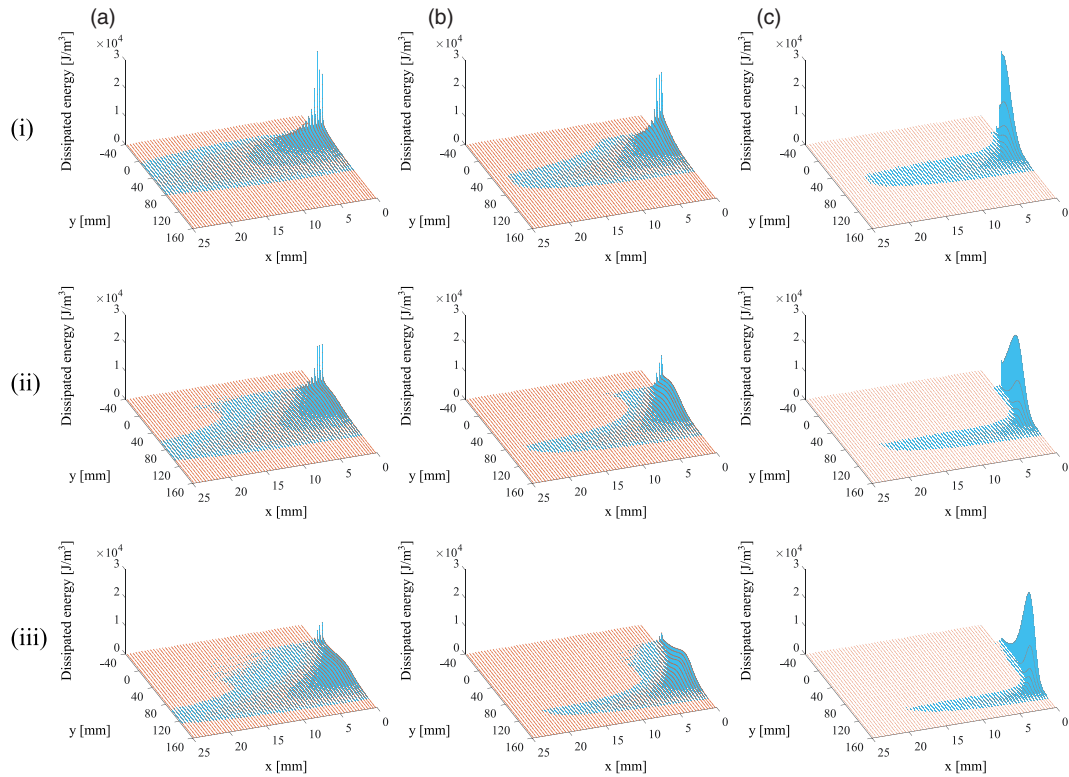
Figure 8. Dissipation maps of the notched specimen using (a) conventional gradient enhancement of $l = 5$ mm and (b) $l = 2$ mm; (c) localizing gradient enhancement of $l = 5$ mm, at the three loading stages of Figure 6(a), (b) and (c) respectively. Only half of the specimen is presented due to symmetry.

The dissipation maps in Figure 8(b) also illustrates a smaller, albeit still obvious, spreading effect compared to Figure 8(a).

The results here thus demonstrate that a smaller length scale parameter helps to reduce the spurious effects, but does not fully resolve the problem. Since the FPZ cannot be captured correctly, its applicability for size effect predictions is still limited. It is also noted that a smaller length scale parameter requires the use of smaller elements for obtaining mesh converged results, hence computationally more expensive.

Remedy with localizing gradient enhancement

The spreading and boundary effects with the conventional gradient enhancement were elaborated in the previous section. Here, the localizing gradient enhancement will be adopted for the same problems to demonstrate its improved performance.

Unnotched specimen

The three-point bend of the unnotched specimen in "Spurious effects with conventional gradient enhancement" section is investigated here, using the same parameters as before ($l = 5$ mm), with the

softening parameter calibrated as $\beta = 60$, to give a structural response that matches well with experimental data in Figure 3(b). A localized damage profile at the end of loading step is also obtained in Figure 3(b), a significant improvement over that of Figure 3(a).

Loading stages following those of Grégoire et al. (2015) are depicted in Figure 3(b). The vertical projection of the incremental dissipation is provided in Figure 4, showing a good match with the meso-scale histograms. The superior performance of the localizing gradient enhancement is better illustrated through the incremental dissipation maps presented in Figure 5(b). Compared to Figure 5(a), a more localized FPZ is obtained here in terms of the bandwidth, as well as being confined to the region at the crack front.

Notched specimen

The three-point bend of the notched specimen with $\lambda = 0.2$ is next considered here with the localizing gradient enhancement. The same parameters as used for the unnotched specimen in this section are adopted here, to give a structural response that match well with the experimental data in Figure 6(c). This already highlights an improved performance with the localizing gradient enhancement, which is in contrast with the earlier analyses using the conventional gradient enhancement where a recalibration is required. As expected, a localized damage profile is obtained at the end of the loading stage. Figure 6(c) also provides the same loading stages as defined in Grégoire et al. (2015).

The projected incremental dissipations in the vertical direction are depicted in Figure 7, which agree well with the meso-scale histograms. Notably, the spurious dissipation spikes at the notch tip are now removed, with a negligible dissipation below the notch tip. In addition to resolving the boundary effect that plagued the conventional gradient enhancement, FPZ is again confined to a region ahead of the crack tip (location of maximum dissipation), as shown in Figure 8(c). Recall that a wrong crack propagation process from the notch tip was obtained with the conventional gradient enhancement in the third section, when compared against the DIC measurements in Alam et al. (2014) for a notch beam of similar geometry ($D = 200$ mm, $\lambda = 0.2$ and span $= 3D$). This crack propagation process is now captured more correctly with the localizing gradient enhancement, i.e. $L_{\text{crack}}/D = 0.175$ at peak load F_{max} (DIC value $= 0.18$), which propagates rapidly to a value of 0.36 at 80% F_{max} post peak (DIC value $= 0.44$), as depicted in Figure 9(b).

Size effect with localizing gradient enhancement

Thus far, the localizing gradient enhancement is shown to describe the evolution and propagation of the FPZ well. Its applicability for capturing both Types 1 and 2 size effects is put to test here, by considering the series of three-point bend tests in Hoover et al. (2013). This is a comprehensive experimental matrix of concrete beams, schematically illustrated in Figure 10, involving four beam depths D, five notch-to-depth ratios λ (including unnotched beams) and a fixed notch width of 1.524 mm (for notched beams). Each beam is of length 2.4D, with a span of 2.176D and a constant out-of-plane thickness of 40 mm. In the experiments, a finite loading and support platen length is utilized to avoid damage therewith. The loading/support platen widths L_S corresponding to each specimen dimension is provided in Table 1. More experimental details can be found in Hoover et al. (2013) and its extension work in Wendner et al. (2015).
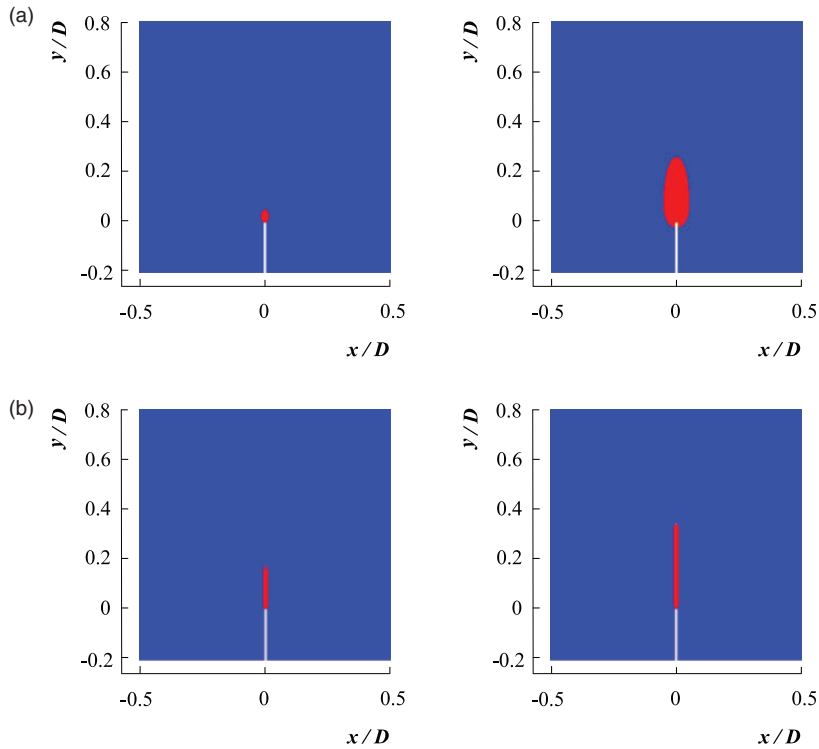
Figure 9. The growth of macro-crack (considered as $\omega > 0.95$) in the notched specimen at F_{max} (left) and $80\%F_{max}$ post peak (right), with (a) conventional gradient enhancement ($l = 5$ mm); (b) localizing gradient enhancement ($l = 5$ mm).
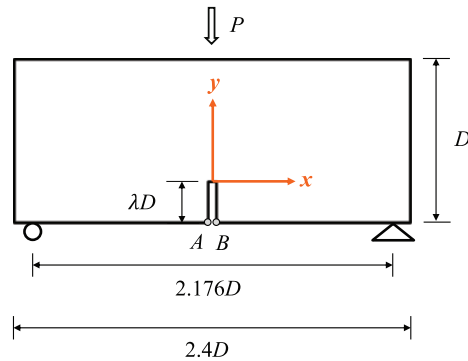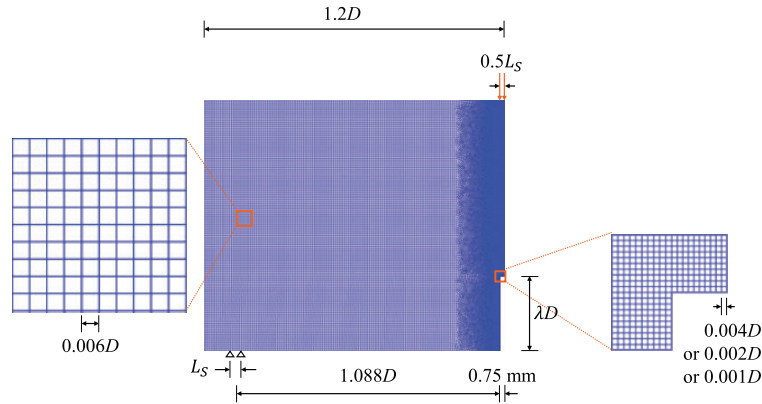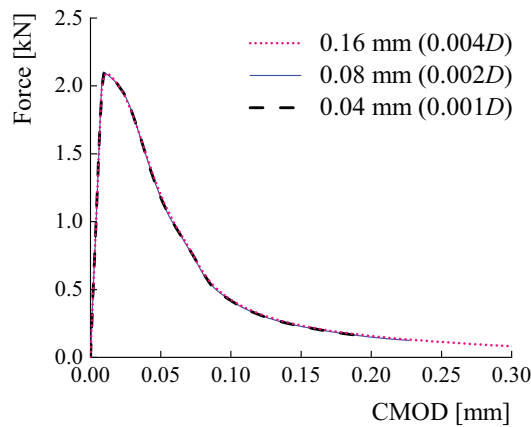

Figure 10. Geometry of the concrete beams under three-point bend tests (Hoover et al., 2013).

Numerical parameters and mesh convergence study

The average values of experimentally measured mechanical properties, i.e., Young's modulus $E = 41.24$ GPa and Poisson's ratio $\nu = 0.172$, are utilized. Adopting a length scale parameter of $l = 5$ mm, the remaining parameters are calibrated from the reference beam ($D = 40$ mm, $\lambda = 0.3$), to

Table 1 Widths of loading/support blocks equipped in the bend tests (Hoover et al., 2013).

Test	Height, D (mm)	Loading/Support block width, L_S (mm)
A	500	60
B	215	25.8
C	93	11.1
D	40	4.8

Figure 11. Mesh and boundary conditions for half of the specimen based on symmetry with respect to *y*-axis.

Figure 12. Mesh convergence for the specimen with $D = 40$ mm and $\lambda = 0.3$ with three different mesh sizes using the localizing gradient enhancement.

give $\kappa_0 = 0.85 \times 10^{-4}$ and $\beta = 130$. These parameters will be used for all beams in this section. The loading/support widths in the simulations follow that of the experimental setup (see Table 1).

The mesh sizes adopted are shown in Figure 11, with a finer mesh close to the notch. For completeness, a mesh refinement check is done for the reference beam by considering three different mesh sizes ($0.004D$, $0.002D$ and $0.001D$) near the notch. The structural responses depicted in
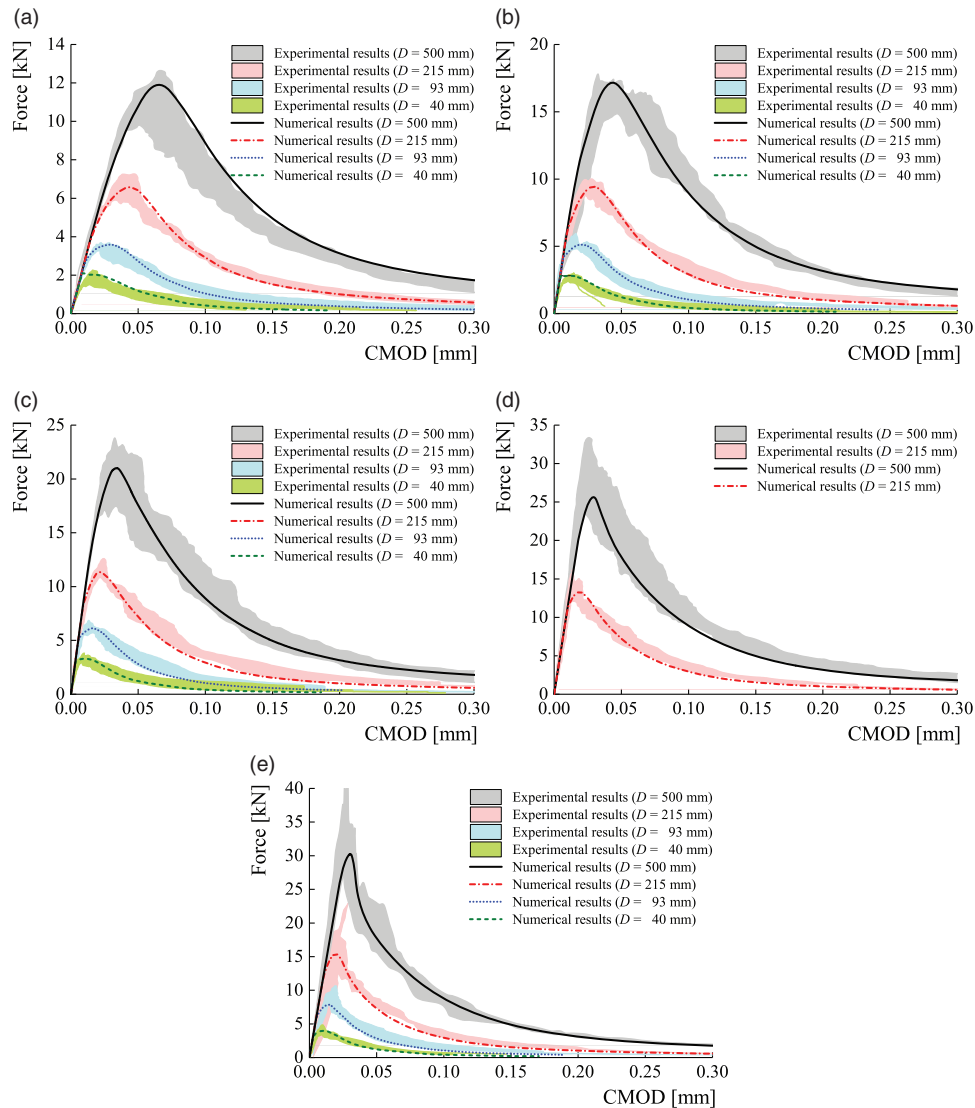
Figure 13. Comparison between experimental data (Hoover et al., 2013) and numerical results using localizing gradient damage enhancement for the concrete specimens with different notch-to-depth ratios: (a) $\lambda = 0.3$; (b) $\lambda = 0.15$; (c) $\lambda = 0.075$; (d) $\lambda = 0.025$ and (e) $\lambda = 0$ (unnotched beam). Shaded regions denote experimental data, lines denote numerical results.

Figure 12 show that mesh convergence is achieved. In the following, a more conservative size of $0.002D$ will be used near the notch for all beams considered.

Results and discussions

The structural responses for all specimen dimensions are compared with the experimental results of Hoover et al. (2013) in Figure 13, using a single set of parameters calibrated from the reference
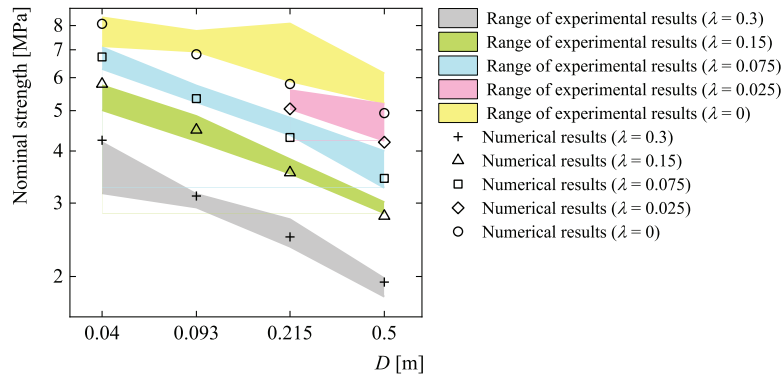
Figure 14. Nominal strength versus beam depth for numerical results using localizing gradient enhancement compared with experimental data (Hoover et al., 2013) for the concrete specimens with different depths *D* and notch-to-depth ratios λ. Shaded regions denote experimental data, scatters denote numerical results.
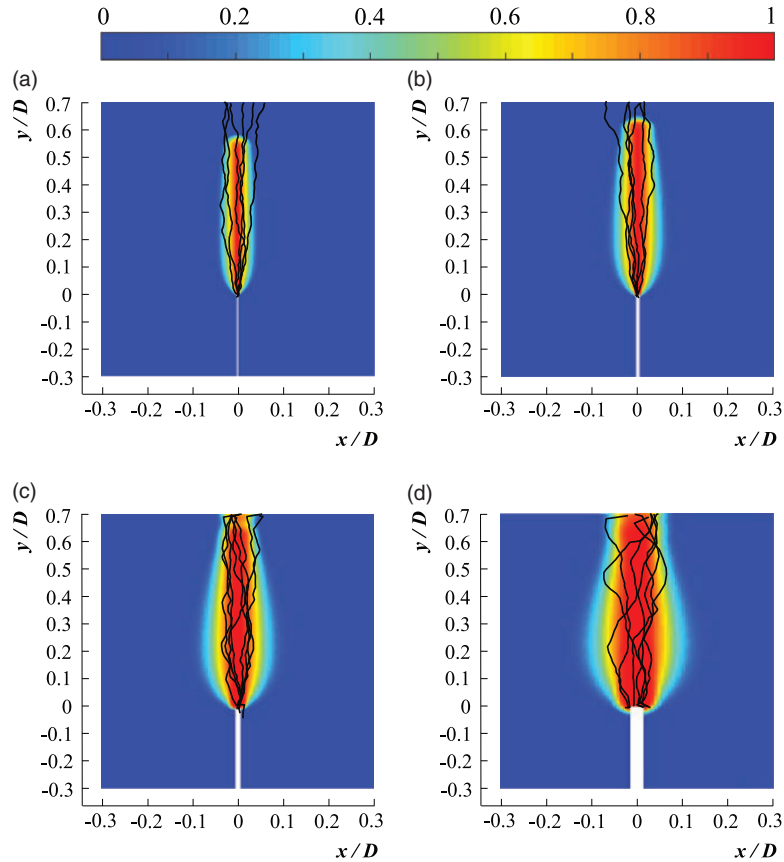

Figure 15. Crack patterns for beams with $\lambda = 0.3$ and (a) $D = 500$ mm; (b) $D = 215$ mm; (c) $D = 93$ mm; (d) $D = 40$ mm. Solid black lines denote average crack paths ($x(y)$) over the ligament depth (y) observed in the experiment (Wendner et al., 2015). Damage profiles from localizing gradient damage enhancement are extracted at CMOD = 0.25 mm.

beam in previous subsection. It is easily observed that both elastic and post-peak softening responses match well with the experimental data for all cases considered. This is a huge improvement compared to the conventional nonlocal enhancement, discussed comprehensively by Grégoire et al. (2013); Havlásek et al. (2016); Marzec and Bobiński (2019a) in the context of integral approach, and is thus not repeated here. A brief presentation with the conventional gradient enhancement was presented by Wosatko et al. (2018), and also demonstrated briefly in third section where the same set of parameters cannot be used for the notched and unnotched beams considered.

Referring to Hoover et al. (2013), the nominal strength of the beam specimen is defined as $\sigma_{N,\max} = 1.5F_{\max}S/(bD^2)$, where $F_{\max}$ is peak load, S is span, b and D are the out-of-plane thickness and depth. As shown in Figure 14, the nominal strength is well captured using the localizing gradient enhancement compared with the experimentally tested data.

As a check, the final damage profiles for the different specimen sizes with $\lambda = 0.3$ are depicted in Figure 15, compared against the experimental crack paths obtained in Wendner et al. (2015). A good agreement is obtained in terms of the numerical and experimental damage bandwidths, which further provides confidence that the localizing gradient enhancement is able to describe the damage processes adequately.

Conclusion

In this contribution, the localizing gradient enhancement (Poh and Sun, 2017) is adopted to resolve the deficiency of conventional nonlocal models in getting accurate predictions on the size effect of quasi-brittle materials. The underlying limitations in a conventional nonlocal enhancement, both integral and gradient approaches, results from an inherent damage diffusion mechanism in the formulation. To better elaborate on this numerical artefact, we distinguish between a spreading effect and a boundary effect in the context of gradient enhancement, in the three-point bend test of concrete beams. Considering first an unnotched beam, a spreading effect is observed with the conventional gradient enhancement, where a very diffused damage process bandwidth is obtained. With a notched beam, a boundary effect is observed where damage diffuses in a non-physically manner to the region below the notch tip, to give a spike in dissipation at the notch tip, in addition to a spreading effect. The combined action of both effects thus delays the initiation of a crack (boundary effect) and retards the crack propagation process (spreading effect).

The localizing gradient enhancement remedies the spurious effects, by restricting the active process zone in front of a crack tip to a finite region, hence resolving the spreading and boundary effects. The projected dissipation profiles in the vertical direction match well with the dissipation histograms from reference meso-scale simulations in Grégoire et al. (2015). Since the crack propagation process is captured adequately with the localizing gradient enhancement, it is able to accurately predict both Type 1 and 2 size effects in the series of three-point bend tests of concrete beams by Hoover et al. (2013), using only a single set of material parameters. The results here, although encouraging, are shown only for tensile dominated fracture. It will be of interest, as part of future work, to investigate the performance of localizing gradient enhancement for other types of experimentally observed size effect, e.g. torsional (Kirane et al. 2016), mixed mode (Garcia-Alvarez et al. 2012) or dynamic fracture (Wang et al. 2018).

Declaration of conflicting interests

ORCID iDs

Yi Zhang 🔟 https://orcid.org/0000-0002-7429-6102
Leong H. Poh 🔟 https://orcid.org/0000-0002-7670-937X

References

Alam SY, Saliba J and Loukili A (2014) Fracture examination in concrete through combined digital image correlation and acoustic emission techniques. *Construction and Building Materials* 69: 232–242.

Al-Rub RA and Voyiadjis GZ (2009) Gradient-enhanced coupled plasticity-anisotropic damage model for concrete fracture: Computational aspects and applications. *International Journal of Damage Mechanics* 18(2): 115–154.

Barbat GB, Cervera M, Chiumenti M, et al. (2020) Structural size effect: Experimental, theoretical and accurate computational assessment. *Engineering Structures* 213: 110555.

Bažant ZP and Le JL (2017) *Probabilistic Mechanics of Quasibrittle Structures: strength, Lifetime, and Size Effect*. New York: Cambridge University Press.

Bažant ZP and Planas J (1997) *Fracture and Size Effect in Concrete and Other Quasibrittle Materials*. New York: CRC Press.

Bažant ZP and Yu Q (2009) Universal size effect law and effect of crack depth on quasi-brittle structure strength. *Journal of Engineering Mechanics* 135(2): 78–84.

Feng DC and Wu JY (2018) Phase-field regularized cohesive zone model (CZM) and size effect of concrete. *Engineering Fracture Mechanics* 197: 66–79.

Forest S (2009) Micromorphic approach for gradient elasticity, viscoplasticity, and damage. *Journal of Engineering Mechanics* 135(3): 117–131.

Forest S (2016) Nonlinear regularization operators as derived from the micromorphic approach to gradient elasticity, viscoplasticity and damage. *Proceedings. Mathematical, Physical, and Engineering Sciences* 472(2188): 20150755.

Garcia-Alvarez VO, Gettu R and Carol I (2012) Analysis of mixed-mode fracture in concrete using interface elements and a cohesive crack model. *Sadhana* 37(1): 187–205.

Geers MGD, de Borst R, Brekelmans WAM, et al. (1998) Strain-based transient-gradient damage model for failure analyses. *Computer Methods in Applied Mechanics and Engineering* 160(1–2): 133–153.

Giry C, Dufour F and Mazars J (2011) Stress-based nonlocal damage model. *International Journal of Solids and Structures* 48(25-26): 3431–3443.

Giry C, Oliver-Leblond C, Ragueneau F, et al. (2014), Non-local model and global-local cracking analysis for the study of size effect. *Computational Modelling of Concrete Structures*. (EURO-C): 255.

Gómez AP, Stolz C, Moës N, et al. (2017) On the capability of the thick level set (TLS) damage model to fit experimental data of size and shape effects. *Engineering Fracture Mechanics* 184: 75–87.

Grassl P, Grégoire D, Solano LR, et al. (2012) Meso-scale modelling of the size effect on the fracture process zone of concrete. *International Journal of Solids and Structures* 49(13): 1818–1827.

Grassl P, Xenos D, Jirásek M, et al. (2014) Evaluation of nonlocal approaches for modelling fracture near nonconvex boundaries. *International Journal of Solids and Structures* 51(18): 3239–3251.

Grégoire D, Rojas-Solano LB and Pijaudier-Cabot G (2013) Failure and size effect for notched and unnotched concrete beams. *International Journal for Numerical and Analytical Methods in Geomechanics* 37(10): 1434–1452.

Grégoire D, Verdon L, Lefort V, et al. (2015) Mesoscale analysis of failure in quasi-brittle materials: comparison between lattice model and acoustic emission data. *International Journal for Numerical and Analytical Methods in Geomechanics* 39(15): 1639–1664.

Havlásek P, Grassl P and Jirásek M (2016) Analysis of size effect on strength of quasi-brittle materials using integral-type nonlocal models. *Engineering Fracture Mechanics* 157: 72–85.

Hoover CG and Bažant ZP (2014) Cohesive crack, size effect, crack band and work-of-fracture models compared to comprehensive concrete fracture tests. *International Journal of Fracture* 187(1): 133–143.

Hoover CG, Bažant ZP, Vorel J, et al. (2013) Comprehensive concrete fracture tests: description and results. *Engineering Fracture Mechanics* 114: 92–103.

Jirásek M (2004) Non-local damage mechanics with application to concrete. *Revue Française de Génie Civil* 8(5–6): 683–707.

Jirásek M, Rolshoven S and Grassl P (2004) Size effect on fracture energy induced by non-locality. *International Journal for Numerical and Analytical Methods in Geomechanics* 28(78): 653–670.

Kirane K, Singh KD and Bažant ZP (2016) Size effect in torsional strength of plain and reinforced concrete. *ACI Structural Journal* 113(6)

Marzec I and Bobiński J (2019a) On some problems in determining tensile parameters of concrete model from size effect tests. *Polish Maritime Research* 26(2): 115–125.

Marzec I and Bobiński J (2019b) Size effect in concrete beams under bending–influence of the boundary layer and the numerical description of cracks. In: *MATEC Web of Conferences*, volume 262. EDP Sciences, p. 10008.

Mazars J and Pijaudier-Cabot G (1989) Continuum damage Theory - Application to concrete. *Journal of Engineering Mechanics* 115(2): 345–365.

Moazzami M, Ayatollahi MR and Akhavan-Safar A (2020) Assessment of the fracture process zone in rocks using digital image correlation technique: the role of mode-mixity, size, geometry and material. *International Journal of Damage Mechanics* 29(4): 646–666.

Nguyen GD (2011) A damage model with evolving nonlocal interactions. *International Journal of Solids and Structures* 48(10): 1544–1559.

Nguyen GD and Bui HH (2020) A thermodynamics-and mechanism-based framework for constitutive models with evolving thickness of localisation band. *International Journal of Solids and Structures* 187: 100–120.

Nguyen VD, Wu L and Noels L (2019) A micro-mechanical model of reinforced polymer failure with length scale effects and predictive capabilities. validation on carbon fiber reinforced high-crosslinked rtm6 epoxy resin. *Mechanics of Materials* 133: 193–213.

Peerlings RHJ, de Borst R, Brekelmans WAM, et al. (1996) Gradient enhanced damage for quasi-brittle materials. *International Journal for Numerical Methods in Engineering* 39(19): 3391–3403.

Peerlings RHJ, de Borst R, Brekelmans WAM, et al. (1998) Gradient-enhanced damage modelling of concrete fracture. *Mechanics of Cohesive-Frictional Materials* 3(4): 323–342.

Peerlings RHJ, Geers MGD, de Borst R, et al. (2001) A critical comparison of nonlocal and gradient-enhanced softening continua. *International Journal of Solids and Structures* 38(44–45): 7723–7746.

Pijaudier-Cabot G and Bažant ZP (1987) Nonlocal damage theory. *Journal of Engineering Mechanics* 113(10): 1512–1533.

Poh LH and Sun G (2017) Localizing gradient damage model with decreasing interactions. *International Journal for Numerical Methods in Engineering* 110(6): 503–522.

Sarkar S, Singh IV, Mishra BK, et al. (2019) A comparative study and abaqus implementation of conventional and localizing gradient enhanced damage models. *Finite Elements in Analysis and Design* 160: 1–31.

Seetharam SC, Laloy E, Jivkov A, et al. (2019) A mesoscale framework for analysis of corrosion induced damage of concrete. *Construction and Building Materials* 216: 347–361.

Simone A, Askes H and Sluys LJ (2004) Incorrect initiation and propagation of failure in non-local and gradient-enhanced media. *International Journal of Solids and Structures* 41(2): 351–363.

Sun G and Poh LH (2016) Homogenization of intergranular fracture towards a transient gradient damage model. *Journal of the Mechanics and Physics of Solids* 95: 374–392.

Voyiadjis GZ and Kattan PI (2009) A comparative study of damage variables in continuum damage mechanics. *International Journal of Damage Mechanics* 18(4): 315–340.

Wang X, Zhang S, Wang C, et al. (2018) Experimental investigation of the size effect of layered roller compacted concrete (rcc) under high-strain-rate loading. *Construction and Building Materials* 165: 45–57.

Wang Z, Shedbale AS, Kumar S, et al. (2019) Localizing gradient damage model with micro inertia effect for dynamic fracture. *Computer Methods in Applied Mechanics and Engineering* 355: 492–512.

Wendner R, Vorel J, Smith J, et al. (2015) Characterization of concrete failure behavior: a comprehensive experimental database for the calibration and validation of concrete models. *Materials and Structures* 48(11): 3603–3626.

Wosatko A, Pamin J and Winnicki A (2018) Numerical prediction of deterministic size effect in concrete bars and beams. In: *Computational Modelling of Concrete Structures: Proceedings of the Conference on Computational Modelling of Concrete and Concrete Structures (EURO-C 2018), Bad Hofgastein, Austria.* New York: CRC Press, pp. 447–456.

Xu Y, Biswas R and Poh LH (2020) Modelling of localized ductile fracture with volumetric locking-free tetrahedral elements. *International Journal for Numerical Methods in Engineering* 121(12): 2626–2654.

Xu Y and Poh LH (2019) Localizing gradient-enhanced rousselier model for ductile fracture. *International Journal for Numerical Methods in Engineering* 119(9): 826–851.

Appendix 1: Numerical framework (plane stress)

The numerical framework is adapted from Poh and Sun (2017). To facilitate the implementation, all expressions are presented in Voigt notations.

The basic two variables, $\underline{u}$, $\tilde{e}$, can be discretized as

$$\underset{2\times 1}{\underline{u}} = \underset{2\times 16}{\underline{N_u}} \, \underset{16\times 1}{\underline{a_u}}, \quad \tilde{e} = \underset{1\times 4}{\underline{N_e}} \, \underset{4\times 1}{\underline{a_e}} \tag{9}$$

where $\underline{N_u}$ and $\underline{N_e}$ are quadratic and linear shape functions respectively; $\underline{a_u}$ and $\underline{a_e}$ are the matrices of the nodal degrees of freedom.

The gradient terms, $\underline{\varepsilon}$ and $\underline{\nabla}\tilde{e}$, are thus discretized as

$$\underset{3\times 1}{\underline{\varepsilon}} = \underset{3\times 16}{\underline{B_u}} \, \underset{16\times 1}{\underline{a_u}}, \quad \underset{2\times 1}{\underline{\nabla}\tilde{e}} = \underset{2\times 4}{\underline{B_e}} \, \underset{4\times 1}{\underline{a_e}} \tag{10}$$

where $\underline{B_u}$ and $\underline{B_e}$ are the gradient operators for displacement and damage strain.

The constitutive relationship for $\boldsymbol{\sigma}$ is given by

$$\boldsymbol{\sigma} = (1 - \omega)\boldsymbol{\mathcal{C}} : \boldsymbol{\varepsilon} \tag{11}$$

Performing a consistent linearization of the stress quantities and ignoring the contribution of higher-traction, the weak form of the governing equations at the global level is reduced to the following equality

$$\int \underline{B_u^{\mathrm{T}}} \mathrm{d}\underline{\sigma} \, dv = \int \underline{N_u^{\mathrm{T}}} \underline{t} \, da - \int \underline{B_u^{\mathrm{T}}} \underline{\sigma} \, dv \tag{12a}$$

$$\int \underline{N_e^{\mathrm{T}}} \mathrm{d}\tilde{\sigma} + \underline{B_e^{\mathrm{T}}} \mathrm{d}\underline{\tilde{\xi}} \, dv = \int -\underline{N_e^{\mathrm{T}}} \tilde{\sigma} - \underline{B_e^{\mathrm{T}}} \underline{\tilde{\xi}} \, dv \tag{12b}$$

The numerical framework can thus be written as

$$\begin{bmatrix} \underline{K_{uu}} & \underline{K_{ue}} \\ \underline{K_{eu}} & \underline{K_{ee}} \end{bmatrix} \begin{bmatrix} \underline{\mathrm{da}_u} \\ \underline{\mathrm{da}_e} \end{bmatrix} = \begin{bmatrix} \underline{F_u} \\ \underline{F_e} \end{bmatrix} \tag{13}$$

where at the element level using a Rankine equivalent strain measure in plane stress condition, the sub matrices are given as

$$\underset{16\times16}{\underline{K_{uu}}} = \int_{elt} \underset{16\times3}{\underline{B}_u^{\mathrm{T}}} (1-\omega) \underset{3\times3}{\underline{C}} \underset{3\times16}{\underline{B}_u} \, \mathrm{d}v,$$

$$\underset{16\times4}{\underline{K_{ue}}} = \int_{elt} \underset{16\times3}{\underline{B}_u^{\mathrm{T}}} \left(-\frac{\partial \omega}{\partial \kappa} \underset{3\times3}{\underline{C}} \underset{3\times1}{\underline{\varepsilon}} \right) \underset{1\times4}{\underline{N}_e} \, \mathrm{d}v,$$

$$- \qquad \underset{4\times16}{\underline{K_{eu}}} = \int_{elt} \underset{4\times1}{\underline{N}_e^{\mathrm{T}}} \left(-\underset{1\times3}{\frac{\partial e^{\mathrm{T}}}{\partial \varepsilon}} \right) \underset{3\times16}{\underline{B}_u} \, \mathrm{d}v,$$

$$\underset{4\times4}{\underline{K_{ee}}} = \int_{elt} \left[\left(\underset{4\times1}{\underline{N}_e^{\mathrm{T}}} + \underset{4\times2}{\underline{B}_e^{\mathrm{T}}} l^2 \frac{\partial g}{\partial \kappa} \underset{2\times1}{\nabla\tilde{e}} \right) \underset{1\times4}{\underline{N}_e} + \underset{4\times2}{\underline{B}_e^{\mathrm{T}}} g l^2 \underset{2\times4}{\underline{B}_e} \right] \mathrm{d}v,$$

$$\underset{16\times1}{\underline{F_u}} = \int_{elt} \underset{16\times2}{\underline{N}_u^{\mathrm{T}}} \underset{2\times1}{\underline{t}} \, \mathrm{d}a - \int \underset{16\times3}{\underline{B}_u^{\mathrm{T}}} \underset{3\times1}{\underline{\sigma}} \, \mathrm{d}v, \underset{4\times1}{\underline{F_e}} = \int_{elt} \left(-\underset{4\times1}{\underline{N}_e^{\mathrm{T}}} (\tilde{e}-e) - \underset{4\times2}{\underline{B}_e^{\mathrm{T}}} g l^2 \underset{2\times1}{\nabla\tilde{e}} \right) \mathrm{d}v$$

Appendix 2: Determination of dissipation

Following the dissipation inequality principle of the localizing gradient enhancement (Poh and Sun 2017), the dissipated energy for the entire domain is given as

$$\mathcal{D} = \frac{1}{2} \int \int (\boldsymbol{\varepsilon} : \mathcal{C} : \boldsymbol{\varepsilon}) \, \mathrm{d}\omega \, \mathrm{d}v \tag{14}$$

Since the numerical framework is in 2 D, the computed dissipation is obtained per unit out of plane thickness. The incremental dissipation $\Delta\mathcal{D}$ in a single element at each loading step is obtained as

$$\Delta\mathcal{D} = \frac{1}{2}\boldsymbol{\varepsilon} : \mathcal{C} : \boldsymbol{\varepsilon} A \Delta\omega \tag{15}$$

where $\Delta\omega$ is the damage increment between two loading steps, and A is the element in-plane area.

Projection of dissipation in the vertical direction

To compute the projection of dissipation in the vertical direction (along specimen ligament), the region of interest is discretized into n rows which are perpendicular to the y-axis, as shown in Figure 16. The length of the ligament is determined from the notch tip to the top surface of the beam specimen along the vertical direction (y-axis). For simplicity, the width of each row, a, is set to
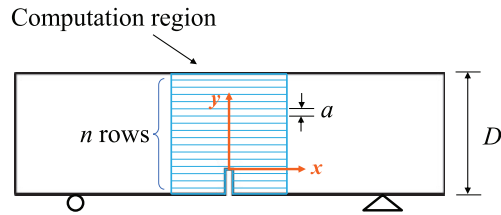
Figure 16. Discretization of "region of interest" to compute the projection of dissipation in the vertical direction.

be the same as the mesh size. All elements in the same row can thus be grouped together. The region of interest should be large enough so that the entire damaged area contributes towards the determination of dissipation.

At each loading step, the total incremental dissipation (per unit out of plane thickness) of an element (E_A) is obtained by the volumetric integration of $\Delta\mathcal{D}$. The dissipation per unit area for each row, projected in the vertical direction, is thus obtained as by summing up the total incremental dissipation from all elements of the same row, divided by the element height a. Note that a convergence check is necessary to ensure that the loading step is small enough, such that a converged dissipation map is obtained.

Dissipation map

The dissipation density of each element is computed as

$$E_v = \frac{\Delta\mathcal{D}}{A} \tag{16}$$

The value in (16) denotes the average volumetric incremental dissipation density in joule per cubic meters. This is plotted at the mid-point of each element to give the dissipation map.